# Conditional stochastic inversion of common-offset GPR reflection data

Zhiwei Xu[1,2,*], James Irving[2], Yu Liu[2], Peimin Zhu[1], and Klaus Holliger[2]

[1] Institute of Geophysics and Geomatics, China University of Geosciences, Wuhan, China
[2] Institute of Earth Sciences, University of Lausanne, Lausanne, Switzerland

[*] Corresponding author, zhiwei.xu@cug.edu.cn

Final accepted version of manuscript GEO-2020-0639.R1 for Geophysics*
Special Issue on Hydrogeophysics

*Please note that this paper represents an extended and complete version of the following work that has been accepted for presentation at the SEG 2020 conference:

Xu, Z., J. Irving, P. Zhu, and K. Holliger, 2020, Conditional stochastic inversion of common-offset GPR reflection data: SEG Technical Program Expanded Abstracts.

March 27, 2021

## Abstract

We present a stochastic inversion procedure for common-offset ground-penetrating radar (GPR) reflection measurements. Stochastic realizations of subsurface properties that offer an acceptable fit to GPR data are generated via simulated annealing optimization. The realizations are conditioned to borehole porosity measurements available along the GPR profile, or equivalent measurements of another petrophysical property that can be related to the dielectric permittivity, as well as to geostatistical parameters derived from the borehole logs and the processed GPR image. Validation of our inversion procedure is performed on a pertinent synthetic data set and indicates that the proposed method is capable of reliably recovering strongly heterogeneous porosity structures associated with surficial alluvial aquifers. This finding is largely corroborated through application of the methodology to field measurements from the Boise Hydrogeophysical Research Site near Boise, Idaho, USA.

Keywords: ground-penetrating radar; aquifer heterogeneity; stochastic inversion; water content; simulated annealing; conditional simulation

## Introduction

Adequate characterization of the spatial heterogeneity of the vadose and/or saturated zones is a prerequisite for the reliable prediction of groundwater flow and contaminant transport in the subsurface. As such, it represents a key objective of many hydrogeological studies (e.g., Salamon et al., 2007; Hu et al., 2009; Cardiff et al., 2013; Maliva, 2016). Traditionally, this objective is approached through local borehole-based studies and larger-scale hydraulic tests. However, the associated gap in terms of spatial resolution and coverage can render an integrated interpretation difficult (e.g., Kobr et al., 2005; Leven and Dietrich, 2006; Gueting et al, 2015). This problem can be alleviated through targeted geophysical measurements (e.g., Rubin and Hubbard, 2006; Hubbard and Linde, 2010; Binley et al., 2015; Romero-Ruiz et al., 2019).

One geophysical method that has attracted significant interest with regard to subsurface hydrogeological studies is surface-based ground-penetrating radar (GPR) reflection profiling. This method has the potential to provide images of shallow subsurface structure with extremely high spatial resolution in comparison with other applied geophysical techniques, and a number of previous studies have investigated how such reflection images might be used in the context of aquifer characterization (e.g., Annan, 2005; Blindow, 2006; and references therein). Because the corresponding data tend to be acquired in bi-static mode with a small constant offset between the transmitting and receiving antennae, one important challenge associated with typical GPR reflection measurements is that they do not readily provide detailed information

on the spatial distribution of petrophysical properties in the probed subsurface region. This is of key interest as the underlying high-frequency electromagnetic wave propagation phenomena are largely governed by the dielectric permittivity, which is highly sensitive to soil water content and thus to soil texture and porosity above and below the water table, respectively (e.g., Knight, 2001). Although the analysis of diffraction hyperbolas in common-offset GPR data may be used to obtain useful information on the permittivity distribution (e.g., Mount et al., 2014; Yuan et al., 2019), the results are strongly limited in terms of spatial resolution and the method inherently requires a high density of diffractions throughout the GPR profile to be reliable.

To address the above limitation and recover detailed information on the dielectric properties of the probed subsurface from reflection GPR measurements, a variety of approaches have been developed. The vast majority of these rely upon the acquisition of multi-offset data, whereby multiple receiver antenna positions are considered for each transmitter antenna position in an analogous manner to seismic reflection surveying (Forte and Pipan, 2017). The corresponding measurements can then be examined using a variety of different techniques, which include quantification of reflector moveout and reflection tomographic approaches (e.g., Greaves et al., 1996; Bradford et al., 2009; Mangel et al., 2020), amplitude-versus-offset (AVO) analysis (e.g., Bradford and Deeds, 2006; Deparis and Garambois, 2009), and waveform inversion (e.g., Lavoué et al., 2014; Babock and Bradford, 2015). While all of these approaches can provide important information on the spatial distribution of the

subsurface dielectric permittivity, and to a lesser extent the electrical conductivity, one important drawback is that the acquisition of multi-offset GPR data for lower-frequency geological applications is time-consuming and logistically cumbersome, and is thus not routinely done. Indeed, lower-frequency GPR surveys typically involve only a single transmitter and receiver antenna, meaning that multi-offset survey time will increase by a factor equal to the number of desired offsets when compared to a common-offset acquisition. Further, methods such as reflection tomography, which rely upon ray theory and the use of traveltimes to reconstruct the permittivity distribution, are well known to suffer from limited spatial resolution. Finally, large uncertainties associated with GPR antenna radiation patterns in complex near-surface media mean that methods like AVO analysis or full-waveform inversion, which require accurate signal amplitudes, may be adversely affected.

If suitable borehole measurements, such as porosity or dielectric permittivity logs, are available for calibration along the GPR profile, one promising alternative for the recovery of detailed electrical property information from common-offset reflection GPR measurements is impedance inversion. In this regard, Schmelzbach et al. (2012) present a workflow to recover spatially distributed electromagnetic impedance, which is closely related to soil dielectric permittivity and water content, from reflection GPR data. Their approach involves sparse-spike deconvolution of an amplitude-corrected and migrated GPR image, followed by band-limited integration and scaling, whereby the low-frequency component of the impedance variability, which is not possible to

recover from the noisy GPR data alone, is derived from direct-push logs acquired along the profile. Zeng et al. (2015) and Liu et al. (2018) use similar approaches to recover water content from common-offset GPR profiles in complex environments and to characterize buried archaeological remains, respectively.

In this paper, we complement and extend previous work on the determination of high-resolution subsurface properties from common-offset reflection GPR measurements with the aim of addressing one important limitation. This is the fact that the approaches developed to date are deterministic in nature and therefore provide only a single solution to an inverse problem that is well known to be highly non-unique due to the heterogeneous subsurface environment and complex physics associated with high-frequency electromagnetic wave propagation. A single deterministic solution makes an assessment of the inferred subsurface models difficult, notably with regard to their uncertainties, and poses a strong limitation on their utility in hydrogeological investigations where groundwater flow and contaminant transport must be evaluated within a statistical, risk-based framework. To this end, we consider the impedance-type inversion of surface-based common-offset GPR reflection data from a stochastic perspective, whereby we seek to match observed radargrams to spatial distributions of subsurface properties that honor, a priori, pertinent in situ information derived from borehole-type measurements as well as prescribed geostatistical constraints. This is done via conditional geostatistical simulation within a stochastic optimization procedure, the repeated application of which allows for the generation of multiple

acceptable models in order to explore and quantify uncertainty (Xu et al., 2020b). Additional advantages of our approach are that realistic lateral continuity is guaranteed in the inversion results and that the accumulation of errors, associated with the along-trace integrations performed in traditional impedance inversion approaches, is avoided.

The paper proceeds as follows. We begin by describing the methodological foundations of our proposed approach. Next, we proceed to assess its viability on a pertinent synthetic case study. Finally, we apply the approach to a field data set from the Boise Hydrogeophysical Research Site (BHRS), Idaho, USA.

## Methodology

Our inversion method assumes the availability of at least one high-resolution borehole or direct-push log of the dielectric permittivity, or a closely related petrophysical property, along the GPR profile that can be used to condition the generation of stochastic subsurface property realizations. This is done within a global optimization loop in order to fit the recorded GPR reflection waveforms. In the current study, we assume full water saturation and perform all analyses in terms of subsurface porosity, meaning that borehole porosity logs are taken to be available and the relationship between GPR velocity and porosity is assumed known via a suitable petrophysical transform. Note, however, that the generalization of our methodology to work with GPR velocity and/or cases with partial water saturation is straightforward.

The steps involved in our inversion procedure to produce a single subsurface

porosity realization are schematically illustrated in Figure 1. Uncertainty can be assessed by running the procedure multiple times and examining the corresponding ensemble of realizations. The overall inversion methodology can be broken down into four major components:

(1) estimating a set of 2D autocovariance parameters that we assume adequately describe the stochastic variability of porosity in the probed subsurface region;

(2) generating a stochastic porosity realization honoring these parameters and conditioned to the borehole or direct-push porosity log measurements;

(3) calculating the corresponding synthetic reflection GPR profile and evaluating its misfit with the field GPR measurements; and

(4) applying simulated annealing (SA) optimization by iterating over steps (2) and (3) to find a porosity realization that honors the estimated stochastic subsurface structure, the borehole porosity log data, and the common-offset GPR reflection measurements.

These components are described in further detail in the subsections below.

**Estimation of subsurface stochastic parameters**

We assume that the stochastic variability of subsurface porosity can be adequately captured by a Gaussian two-point geostatistical model. This assumption is generally considered to be valid for a given hydrogeological unit (e.g., Kelkar and Perez, 2002; Dafflon et al., 2009). For the parameterization of this model, we consider the so-called von Kármán autocorrelation function which, due to its versatility, has been used for a

wide variety of research objectives, such as seafloor morphology quantification (e.g., Goff and Jordan, 1988), borehole data analysis (e.g., Dolan and Bean, 1997; Jones and Holliger, 1997), numerical simulations of wave propagation (e.g., Frankel and Clayton, 1986; Hartzell et al., 2010), and aquifer characterization (e.g., Tronicke and Holliger, 2005; Dafflon et al., 2009). In 2D and for anisotropic porosity heterogeneity aligned along coordinate axes $x$ and $z$, the von Kármán autocorrelation equation takes the following form (e.g., Goff and Jordan, 1988):

$$R_{\theta\theta}(\delta x, \delta z) = \frac{r^{\nu} K_{\nu}(r)}{2^{\nu-1}\Gamma(\nu)} \tag{1}$$

where $R_{\theta\theta}$ is the porosity autocorrelation, $\delta x$ and $\delta z$ are the spatial autocorrelation lags in the $x$- and $z$-directions, respectively, $K_{\nu}(r)$ is the modified Bessel function of the second kind having order $0 \leq \nu \leq 1$, $\Gamma$ is the gamma function, and

$$r = \sqrt{\left(\frac{\delta x}{a_x}\right)^2 + \left(\frac{\delta z}{a_z}\right)^2} \tag{2}$$

is a normalized lag parameter with $a_x$ and $a_z$ denoting the spatial correlation lengths along $x$ and $z$, respectively. Equation 1 defines an anisotropic heterogeneous medium which is self-similar, or fractal, at scales shorter than the correlation lengths. The decay of the autocorrelation function at small lags, and thus the local variability of the associated heterogeneity, is controlled by $\nu$, which is generally referred to as the Hurst number. Values of $\nu$ close to 0 and 1 characterize locally highly complex and smooth fluctuations, respectively, whereas for $\nu$= 0.5, the von Kármán autocorrelation function reduces to its well-known, Brownian-noise-type, exponential equivalent (e.g., Goff and Jordan, 1988).

Variables $a_x$, $a_z$, and $\nu$ parameterize our geostatistical porosity model and must be determined from available data. Following Tronicke and Holliger (2005), we estimate $a_z$ and $\nu$, as well as the porosity mean and variance, from the high-resolution porosity logs available along the GPR profile. Parameter $a_x$ can then be inferred from the GPR data using the inversion approach of Irving et al. (2009), which relates the geostatistical properties of the backscattered wavefield to those of the underlying scattering medium. Specifically, this approach allows for inference of the structural aspect ratio $a_x/a_z$ of the probed subsurface medium (Irving and Holliger, 2010) from which, knowing $a_z$, we can readily determine $a_x$. It is important to note that our use of this procedure inherently assumes the geostatistical structures of GPR velocity and porosity to be identical. This is reasonable in saturated soils given the approximately linear relationship between GPR velocity and water content over the range of porosities typically encountered in near-surface materials (e.g., Irving et al., 2009; Xu et al, 2020a).

**Generation of conditional porosity realizations**

The core of our inversion procedure involves the generation of stochastic realizations of the subsurface porosity field that (1) honor the geostatistical parameters inferred from the borehole porosity logs and common-offset GPR reflection data, and (2) fit exactly the borehole porosity measurements, which are treated as hard constraints. These realizations are then tested with regard to how well they allow us to predict the observed GPR reflection data, and are iteratively perturbed within a SA optimization loop to

generate a single inversion output realization (Figure 1).

We generate unconditional stochastic realizations using the fast Fourier transform moving average (FFT-MA) technique (LeRavalec et al., 2000), which is a convenient and attractive implementation of the moving average (MA) geostatistical simulation method of Oliver (1995) in the discrete wavenumber domain. The FFT-MA method has been recognized for its efficiency and flexibility (e.g., Caers, 2007; Le Ravalec-Dupin et al. 2008; de Figueiredo et al. 2018). Any permissible autocovariance model may be considered and, given that the random and deterministic components of the algorithm are separated in the spatial, rather than in the wavenumber, domain, local re-simulations of specific areas of the model grid are possible. The latter cannot be done with standard power spectral simulation techniques (e.g., Ikelle, 1993) and has led to the common application of FFT-MA for stochastic modeling and inversion (e.g., Le Ravalec-Dupin et al., 2004; Le Ravalec and Mouche, 2012; Liang and Marcotte, 2016; Yang and Zhu, 2017; Lauzon and Marcotte, 2019).

From an unconditional FFT-MA-generated realization, which is not constrained to respect the porosity log data at the borehole locations, a corresponding conditional realization can be generated as follows (e.g., Chilès and Delfiner, 2012; Nussbaumer et al., 2019):

$$Z_c(x,z) = Z^*(x,z) + [Z_u(x,z) - Z_u^*(x,z)], \tag{3}$$

where $Z_c$ is the output conditional porosity realization, $Z_u$ is the unconditional realization generated using FFT-MA, and $Z^*$ and $Z_u^*$ the ordinary-kriging-based

porosity estimates based on the log and unconditional simulation values at the borehole locations, respectively.

It is important to note that the conditional porosity simulations that are generated using the above procedure are effectively parameterized by a Gaussian white noise vector in the spatial domain, whose individual elements correspond to each location in the model grid. Re-simulating the values in this noise vector will produce different stochastic realizations, all of which honor the underlying von Kármán geostatistical model and the porosity values at the borehole locations. We exploit this in our SA optimization procedure, wherein conditional realizations are perturbed by re-simulating a certain percentage of elements in the Gaussian white noise vector. The number of re-simulated points and their location in the model grid govern the magnitude and the local-versus-global nature of the corresponding model perturbation.

**GPR forward model**

To compute the synthetic GPR reflection profile corresponding to a conditional stochastic porosity realization, we use the so-called primary reflectivity section (PRS) model (e.g., Gibson and Levander, 1990; Holliger et al., 1994; Irving et al., 2009), whereby an amplitude-corrected and time-migrated seismic or GPR reflection image $d(x,t)$ is expressed as the convolution of a source wavelet function $w(t)$ with the underlying subsurface reflectivity coefficient field $r(x,t)$:

$$d(x,t) = w(t) * r(x,t), \tag{4}$$

where $t$ is the vertical two-way traveltime and $*$ denotes convolution in time. Assuming that single scattering prevails and that dispersion is absent from the data, equation 4 is widely recognized to provide an adequate model for zero-offset geophysical reflection data (e.g., Yilmaz, 2001). Although the second assumption is only strictly valid for GPR data acquired under perfectly electrically resistive conditions, past experience has shown that this model is able to accommodate the limited dispersion effects associated with low-loss environments for which the GPR method has been conceived (e.g., Irving et al., 2009; Xu et al., 2020a).

Reflection coefficients as a function of two-way travel time in equation 4 are obtained from the conditional porosity realization by first transforming it to dielectric permittivity. This is done using the following mixture model for water-saturated media (e.g., Schön, 1998):

$$\sqrt{\varepsilon_r} = \sqrt{\varepsilon_r^s}(1-\phi) + \sqrt{\varepsilon_r^w}\phi, \tag{5}$$

where $\phi$ is the porosity, $\varepsilon_r$ is the relative dielectric permittivity, and $\varepsilon_r^s$ and $\varepsilon_r^w$ are the relative dielectric permittivities of the dry solid matrix and water, respectively, for which we assume values of 4.6 and 80 (e.g., Chan and Knight, 2001). For low-loss media amenable to GPR wave propagation, the high-frequency electromagnetic wave velocity $v$ is related to the relative dielectric permittivity through (e.g., Annan, 2005)

$$v = \frac{c}{\sqrt{\varepsilon_r}} \tag{6}$$

where $c = 3 \times 10^8$ m/s is the speed of light in free space. This equation is used to transform depth into two-way vertical traveltime. Vertical incidence reflection

coefficients in the traveltime domain are then obtained using

$$R = \frac{\sqrt{\varepsilon_{r_1}} - \sqrt{\varepsilon_{r_2}}}{\sqrt{\varepsilon_{r_1}} + \sqrt{\varepsilon_{r_2}}} \tag{7}$$

where indices 1 and 2 refer to the materials above and below an interface, respectively. Equation 7 is applied iteratively to each column of the subsurface dielectric permittivity model to yield $r(x,t)$.

To estimate the GPR source wavelet $w(t)$ from field reflection measurements, we employ the constant phase method (Cui and Margrave, 2014). With this approach, the wavelet's Fourier domain amplitude spectrum is estimated from the GPR data assuming a statistically white series of reflection coefficients, whereas the phase spectrum is estimated based on borehole log measurements. In particular, a series of constant-phase rotations are applied to the amplitude spectrum derived from the GPR data, and each of the corresponding time-domain wavelets is then convolved with the reflectivity calculated from the borehole data. The phase rotation that provides the highest correlation between the resulting synthetic trace and the measured trace at the borehole location is chosen as the estimated wavelet phase. Based on numerous synthetic tests, we have found this approach to provide a reliable enough estimation of the GPR wavelet for use in our stochastic inversion methodology.

**SA optimization**

We wish to find conditional realizations of subsurface porosity, generated using the technique described above, whose corresponding synthetic GPR reflection data offer a

good fit to the field GPR measurements. To this end, we build on previous work (e.g., Tronicke and Holliger, 2005; Dafflon et al., 2009, Lauzon and Marcotte, 2019) and use SA, a directional Monte-Carlo-type approach, to iteratively perform the optimization. The objective function to be minimized is the simple sum-of-squares error

$$O = \sum_{k} \sum_{j} \left( d^{syn}(x_j, t_k) - d^{obs}(x_j, t_k) \right)^2, \tag{8}$$

where $d^{syn}$ and $d^{obs}$ denote the synthetic and field reflection GPR profiles, respectively, and indices $j$ and $k$ sum over the number of points per trace and number of traces in the data, respectively.

We begin the SA procedure with a conditional porosity realization generated using a fully random vector of FFT-MA uncorrelated Gaussian noise elements, which is unconditionally accepted in the first iteration after the corresponding objective function value is evaluated. In subsequent iterations, a new conditional realization is created by re-simulating a randomly chosen subset of elements in the Gaussian noise vector, where the number of points in the subset $N_i$ is given by

$$N_i = N_0 \cdot \gamma^i. \tag{9}$$

Here, $i$ denotes the SA iteration number, $N_0$ is the total number of vector elements, and constant $\gamma$ determines the rate at which the size of the model perturbation decreases as the iterations proceed (Lauzon and Marcotte, 2019). In this way, and similar to the effect of the temperature parameter discussed below, exploration of the model space is encouraged in the beginning of the SA algorithm, whereas exploitation is encouraged towards the end. Note that when the value of $N_i$ in equation 9 becomes

less than 1, only a single vector element is re-simulated. For both the synthetic and field examples presented in the next section, $\gamma$ was set to an empirically determined value of 0.97.

After evaluating the objective function for the perturbed porosity realization using equation 8, the realization is either accepted or rejected according to a stochastic decision rule, whose probability of acceptance is given by

$$P_i^{acc} = \begin{cases} 1, & \text{if } O_i < O_{i-1} \\ \exp\left(-\left(\dfrac{O_i - O_{i-1}}{T_i}\right)\right), & \text{otherwise} \end{cases} \tag{10}$$

where $T_i$ is a unitless "temperature" parameter whose progressive decrease with increasing number of iterations defines the "cooling schedule" of the optimization process. Higher $T_i$ values imply a greater probability of accepting random model perturbations that do not decrease the value of the objective function, which tends to encourage greater exploration of the model space. Here we use

$$T_i = T_0 \cdot \alpha^i, \tag{11}$$

where $T_0$ is the intial temperature and $\alpha$ is the temperature reduction factor, whose value also controls the balance between exploration and exploitation as the SA iterations proceed. Based on the arguments presented in Johnson et al. (1991), $T_0$ was set to a value of $1.5\text{x}10^{10}$ in our synthetic example and to a value of $1\text{x}10^{8}$ for our field study. The parameter $\alpha$ was set equal to 0.95 in both cases.

For simplicity, SA iterations are continued in our inversion algorithm until a prescribed maximum number of iterations is reached. For our synthetic example, setting

the maximum number of iterations to 350 was found to yield an acceptable fit to the observed GPR traces given the prescribed errors in the data. For the field study, a maximum number of 320 iterations was considered based on similar arguments.

## Results

### Synthetic study

To assess the viability of our proposed approach, we first apply it to a synthetic case study. The underlying "true" porosity model, which aims to emulate conditions in a heterogeneous alluvial aquifer, is shown in Figure 2 and was created using the FFT-MA unconditional simulation method described previously. It is based upon the porosity distribution considered in Tronicke and Holliger (2005) and is characterized by a von Kármán autocovariance function having a *v*-value of 0.3, a mean porosity value of 0.19, and a standard deviation of 0.026. The horizontal and vertical correlation lengths used in the model generation process are $a_x$ = 133 m and $a_z$ = 13 m, respectively. This implies that the resulting stochastic medium is pervasively self-similar and, hence, exhibits the typical combination of small- and large-scale heterogeneity observed in alluvial aquifers (Tronicke and Holliger, 2005). In this context, it is interesting to note that the larger-scale heterogeneities in Figure 2, such as the high-porosity channel running across the model, assume a quasi-deterministic appearance. We consider the presence of three boreholes, located at lateral distances of 5, 15, and 27 m from the left model edge, along which high-resolution porosity logs are assumed to be available. The

porosity data from the left- and right-hand boreholes are used as conditioning information in our inversions, whereas the data from the center borehole are used for validation purposes.

Using equation 5, the porosity realization in Figure 2 was transformed into a distribution of subsurface relative dielectric permittivity and a synthetic common-offset GPR reflection survey was simulated using the gprMax software, which solves Maxwell's equations using the finite-difference time-domain (FDTD) method (Giannopoulos, 2005). The values of the electrical conductivity and relative magnetic permeability were set to 1 mS/m and 1, respectively. For the FDTD modeling, we used a transmitter-receiver antenna separation of 0.5 m and a Ricker source wavelet with a center frequency of 100 MHz. Synthetic GPR traces, sampled every 0.5 ns, were generated every 0.1 m along the profile.

After adding 2% uncorrelated Gaussian noise, the synthetic GPR data were subjected to a standard processing sequence consisting of (1) 10-300 MHz bandpass filtering to remove noise along with the low-frequency transient or "wow" upon which the GPR reflections are superimposed; (2) application of a smooth time-varying gain based on the inferred average energy decay curve to compensate for the geometrical spreading of energy along with scattering and transmission losses; and (3) 2D f-k time migration (Stolt, 1978) using a constant velocity of 0.09 m/ns. This velocity, which roughly corresponds to the average GPR velocity of the model, was found to optimally focus hyperbolic diffraction events. In Figure 3, we show the resulting processed GPR

image together with the source wavelet that was estimated from these data using the constant phase method and the true source wavelet for reference. We see that, in the GPR image, there are no apparent general trends in signal amplitude with time, which suggests that our choice of smooth gain function has effectively compensated for spreading and scattering/transmission losses in the data while leaving the relative reflection amplitudes intact. The latter is critical for an effective use of the PRS convolution model described previously. With regard to the estimated GPR source wavelet, we see that the constant phase method yields a result that is close in form to the true source wavelet (Figure 3b), meaning that it should allow for reliable forward modeling of predicted data in our inversion procedure.

The processed GPR data shown in Figure 3a, together with the high-resolution porosity information from the left- and right-hand boreholes, were subjected to the conditional stochastic inversion workflow outlined in Figure 1. Based on geostatistical analysis of the porosity log data, we estimated a mean and standard deviation of 0.193 and 0.0259, respectively, and a Hurst number of $\nu$ = 0.30. These estimates are all close to the true values. Analysis of the GPR image using the stochastic inversion methodology of Irving et al. (2009) yielded a mean value for the aspect ratio of the subsurface porosity field of 10.5, which is again close to the true value and was used with the considered vertical correlation length of $a_z$ = 13.0 m to obtain a value for the lateral correlation length of $a_x$ = 136.5 m. These results, along with the measured porosity data at the borehole locations, were used to generate conditional porosity

simulations (Figure 4) that were optimized to fit the GPR measurements using SA (Figure 1). Note that only the GPR data beyond 50 ns in time were considered in the inversion procedure in order to avoid the zone containing the direct air and ground arrivals (Figure 3).

In Figure 5 we compare the underlying "true" porosity model from Figure 2 with three output realizations obtained using our inversion methodology, along with maps of the mean and standard deviation of porosity inferred from an ensemble of 100 such realizations. Overall, the conditional stochastic inversion results are seen to faithfully reproduce both the smaller- and larger-scale features of the true porosity heterogeneity, and we observe a close match of the ensemble mean to the target model, even away from the left- and right-hand conditioning borehole locations, all of which suggests that the inversion procedure has successfully converged and that the reflection GPR measurements have greatly helped in characterizing the subsurface porosity distribution. Unsurprisingly, the standard deviation of the output ensemble is highest in the middle of the model domain where borehole conditioning data are not available. Note, however, that the corresponding values ($< 0.012$) are still significantly lower than the global standard deviation of the porosity distribution (0.026), suggesting that the reflection GPR measurements have notably reduced our uncertainty in this region. A zone of higher uncertainty is present near the top of the model because the inversion results were not conditioned to the GPR data for times less than 50 ns.

We compare in Figure 6 the true and inverted results for the central validation

borehole location, in terms of both porosity logs (Figure 6a) and the corresponding GPR traces (Figure 6b). The curves for 100 inversion realizations along with the ensemble mean are shown. Also shown in Figure 6c are the porosity curves at the central borehole location corresponding to 100 conditional stochastic realizations that were not constrained to fit the GPR data. The latter represents the prior in our inversion procedure. We observe in Figure 6a that, overall, the larger-scale trends in the true porosity distribution are well captured by the inversion realizations, in the sense that the mean porosity curve follows reasonably closely the true one. The levels of small-scale variability in the inversion results and the true porosity distribution are also similar. With regard to fitting the GPR data, all of the modeled traces corresponding to the porosity inversion results offer a close match to the observed trace at the validation borehole location (Figure 6b). Finally, in comparing the range of the prior stochastic realizations shown in Figure 6c with that of the inverted realizations in Figure 6a, we see that consideration of the GPR data has significantly reduced our uncertainty with regard to the porosity distribution in the middle of the model domain. Regions where the true porosity distribution falls close to the limits of the range of the inverted realizations, for example between 10 m and 12 m depth, are also seen to be regions where the true porosity is less likely in the context of the considered prior.

## Application to field data

Our proposed stochastic inversion method was applied to GPR reflection measurements from the Boise Hydrogeophysical Research Site (BHRS), which is located on a gravel bar adjacent to the Boise River, near Boise, Idaho, USA (Figure 7). The site contains 13 boreholes in a central area, which has a diameter of ~20 m, and five boreholes near its borders located at distances of ~10 to ~35 m from this central area. The underlying braided-river-type aquifer consists of late Quaternary fluvial deposits dominated by coarse cobbles and sand. These are followed by a layer of red clay, which is situated at ~20 m depth (e.g., Barrash and Clemo, 2002). The depth to the groundwater table varies seasonally between ~2 and ~4 m. Over the past two decades, the site has been extensively used for the testing, validation, and improvement of a wide variety of geophysical and hydrogeological methods for characterizing heterogeneous aquifers (e.g., Tronicke et al., 2004; Bradford et al., 2009; Nichols et al., 2010; Dafflon et al., 2011; Dafflon and Barrash, 2012; Cardiff et al., 2013; Hochstetler et al., 2016).

The considered GPR reflection profile is part of a 3D survey, which was performed in the summer of 1998 using a PulseEkko Pro 100 system (Sensors & Software Inc.) with a nominal antenna center frequency of 100 MHz. The data were collected in common-offset mode using a transmitter-receiver antenna spacing of 1 m. Traces were recorded every 0.2 m along the profile, which is 18 m long and aligned with boreholes C6, A1, and C3 (Figure 7). The time sampling interval was 0.8 ns and, for each recorded GPR trace, 32 vertical stacks were performed to improve the signal-to-noise ratio.

The BHRS GPR data were subjected to a similar processing flow as their synthetic counterparts, which included time-zero and near-offset corrections, dewow filter, smooth time-varying gain based on the observed amplitude decay along each trace, and 2D f-k time migration using a constant velocity of 0.08 m/ns. The latter value was found to optimally focus diffraction events in the data below the water table, and is consistent with the average velocity of saturated sediments at the BHRS determined by Bradford (2009). The processed GPR image, along with the estimated source wavelet, are shown in Figure 8, whereas Figure 9 shows neutron-neutron porosity logs acquired along boreholes C6, A1, and C3, which are located 0.6 m, 9 m, and 16 m from the left edge the GPR profile, respectively (Barrash and Clemo, 2002). Given that the porosity measurements are only available below the groundwater table, we limit our analysis to the saturated part of the probed subsurface region starting at ~2.8 m depth.

As in the synthetic case study, the left- and right-hand borehole logs (C6 and C3) were used for conditioning the stochastic inversion procedure, whereas the central log (A1) was reserved for validation. In this regard, geostatistical analysis of the porosity log data led to an estimated mean and standard deviation of 0.23 and 0.055, respectively, a Hurst number of $\nu$ = 0.35, and a vertical correlation length of $a_z$ = 0.75 m. Along the direction of the considered GPR profile, the stochastic analysis of 3D GPR data from the BHRS of Xu et al. (2020a) using the method of Irving et al. (2009) suggests that a horizontal-to-vertical aspect ratio of 12 is most likely, which implies a lateral correlation length of $a_x$ = 9 m. All of these parameters were used to generate

conditional stochastic porosity realizations that were then optimized to fit the GPR measurements.

Two example realizations obtained with our inversion procedure, along with the mean and standard deviation of an ensemble of 100 such realizations, are shown in Figure 10. As observed previously in the synthetic case study (Figure 5), the inverted models are consistent with each other as well as with the ensemble mean. The values of the ensemble standard deviation are also seen to follow the same overall spatial pattern as those in the synthetic case study. Note, however, that they are higher by approximately a factor of 3.0, indicating greater uncertainty in the subsurface porosity distribution given the provided data.

In Figure 11 we show a comparison of the inverted and observed porosity profiles and corresponding GPR traces along the central borehole A1, as well as porosity curves along this borehole corresponding to the prior distribution assumed in the inversion procedure. We see that, overall, the proposed inversion approach provides a good fit to the observed GPR data, allows for a substantial reduction of uncertainty in porosity compared to the assumed prior distribution, and allows us to adequately reproduce the observed porosity profile to ~6.2 m depth. Between ~6.2 m and ~7.4 m depth, however, we observe in Figure 11a a systematic mismatch between the observed and inverted porosity curves, which finds its clear expression in the fact that the range of the porosity values of the 100 accepted realizations shows no overlap with the observed porosity data. In this context, it is interesting to note that this region is characterized by an

unusually low standard deviation (Figure 10d), which suggests that our inversion procedure found no other means of fitting the observed data.

## Discussion

The systematic bias towards too low estimated porosity values in the lower part of the profile in Figure 11a could potentially be related to (1) inadequacies of the estimated GPR source wavelet; (2) local variations in amplitude decay of the observed GPR data that have not been adequately compensated; (3) problems with the neutron-neutron porosity log in central borehole A1, for example due to borehole enlargements and/or incomplete backfill behind the slotted PVC well casing that locally lead to values that are too high; or (4) local violations of our inherent assumption of statistical stationarity.

While it is quite likely that the estimated source wavelet is to some degree sub-optimal, we would nevertheless expect the resulting mismatches between the inversion result and control data to be spatially more uniform and/or more gradual in their onset than those observed in Figure 11a if the wavelet were the primary problem. Visual inspection of the observed GPR reflection data in Figure 8a does, however, suggest that the amplitudes in the corresponding central region below ~150 ns are systematically weaker than elsewhere in the profile. Preliminary analysis indicates that this local amplitude deficit is not associated with a pronounced increase in signal dispersion and, thus, is unlikely to be indicative of stronger local attenuation, for example due to increased clay content. As such, it may be related to acquisition effects, such as

variations in antenna coupling and/or system performance, which were incompletely compensated in the course of the data processing flow.

To explore the latter possibility, we completely reprocessed the GPR data presented in Figure 8 using a variety of alternative gain functions. While in some cases this helped to raise the amplitudes in the lower parts of the GPR section, it did not allow us to remove the bias in the inferred porosity distribution. In this context, it is important to note that, in the process, we also explored the impact of uncertainties in the source wavelet estimation as well as in the estimated correlation lengths and $\nu$-value. None of these efforts allowed us to significantly reduce the bias. Indeed, the inferred porosity distributions shown in Figure 11a remained remarkably stable, which in turn points to the inherent robustness of our inversion approach.

The peak at ~6.8 m depth in the central A1 borehole porosity log corresponds to an unusually high value, which exceeds the local mean by more than one standard deviation (Barrash and Clemo, 2002). The associated high-porosity region between ~6.2 m and ~7.4 m depth, where our stochastic inversion procedure consistently provides porosity estimates that are too low with regard to the log data, may therefore be a local anomaly. Such an anomaly could, as mentioned above, either be related to borehole enlargements and/or incomplete backfill behind the PVC casing, or it could represent an actual geological feature such as an isolated lens of open-frame gravels. Based on the available data, we are unable to distinguish between these two potential explanations. Conditioning our stochastic inversion procedure to additional porosity

information between boreholes C6 and B3 would evidently help to identify such anomalous zones and reduce, if not eliminate, the observed bias. In this regard, future work should investigate if there exists a link between subsurface lateral correlation lengths and the conditioning borehole spacing required to avoid such problems.

Finally, it is interesting to note that the laterally consistent transition to significantly lower porosities beyond ~6.8 m depth in our inversion results in Figure 10 is consistent with Barrash and Clemo's (2002) interpretation of a transition from a high-porosity layer (Unit 4: mean porosity = 0.22, standard deviation = 0.05) to a low-porosity layer (Unit 3: mean porosity = 0.17, standard deviation = 0.02). This, in turn, illustrates that, while the proposed stochastic inversion approach is unable to account for local statistical non-stationarity, such as the unusually high porosity in the central region between ~6.2 m and ~7.4 m depth, it is robust with regard to laterally consistent changes in the medium properties.

## Conclusions

We have presented a novel conditional stochastic inversion method for surface-based common-offset GPR reflection data. The associated workflow has been validated on a pertinent synthetic data set and applied to field data from the BHRS. While the synthetic test case illustrates the potential of the proposed approach to faithfully infer strongly heterogeneous porosity structures from surface-based GPR reflection measurements, the application to field data shows some local misfit with regard to the control data, the

potential origins of which have been discussed. The current applications of our inversion methodology are 2D and consider full water saturation. However, generalization to 3D and partial water saturation are conceptually straightforward. In this regard, our proposed method has significant potential as the acquisition of 3D multi-offset is too time consuming for most geological applications.

## References


Annan, A. P., 2005, GPR methods for hydrogeological studies in hydrogeophysics, in Y. Rubin and S. Hubbard, eds., Hydrogeophysics: Springer, 185-213.

Babcock, E., and J. H. Bradford, 2015, Reflection waveform inversion of ground-penetrating radar data for characterizing thin and ultrathin layers of nonaqueous phase liquid contaminants in stratified media: Geophysics, 80(2), H1-H11, doi: 10.1190/geo2014-0037.1.

Barrash, W., and T. Clemo, 2002, Hierarchical geostatistics and multifacies systems: Boise Hydrogeophysical Research Site, Boise, Idaho: Water Resources Research, 38(10), 14-1 – 14-18, doi: 10.1029/2002WR001436.

Binley, A., Hubbard, S.S., Huisman, J.A., Revil, A., Robinson, D.A., Singha, K. and Slater, L.D., 2015, The emergence of hydrogeophysics for improved understanding of subsurface processes over multiple scales: Water Resources Research, 51(6), 3837-3866, doi: 10.1002/2015WR017016.

Blindow, N., 2006, Ground Penetrating Radar in Groundwater Geophysics, in Kirsch Reinhard, eds., Groundwater Geophysics: Springer, 226-252.

Bradford, J.H. and Deeds, J.C., 2006. Ground-penetrating radar theory and application of thin-bed offset-dependent reflectivity: Geophysics, 71(3), K47-K57, doi: 10.1190/1.2194524.

Bradford, J. H., W. P. Clement, and W. Barrash, 2009, Estimating porosity with ground-penetrating radar reflection tomography: A controlled 3-D experiment at the Boise Hydrogeophysical Research Site: Water Resources Research, 45(2), 1-11, doi: 10.1029/2008WR006960.

Caers, J., 2007, Comparing the gradual deformation with the probability perturbation method for solving inverse problems: Mathematical Geology, 39(1), 27-52, doi: 10.1007/s11004-006-9064-6.

Cardiff, M., T. Bakhos, P. K. Kitanidis, and W. Barrash, 2013, Aquifer heterogeneity characterization with oscillatory pumping: Sensitivity analysis and imaging potential. Water Resources Research: 49(9), 5395-5410, doi:10.1002/wrcr.20356.

Chan, C. Y., and R J. Knight, 2001, Laboratory measurements of electromagnetic wave velocity in layered sands: Water Resources Research, 37(4), 1099-1105, doi: 10.1029/2000WR900356.

Chilès, J., and P. Delfiner, 2012, Geostatistics: Modeling Spatial Uncertainty, 2nd ed: John Wiley & Sons.

Claerbout, J.F., 1985, Imaging the Earth's Interior: Blackwell Scientific Publications.

Cui, T., and G. F. Margrave, 2014, Seismic wavelet estimation: University of Calgary CREWES Project Research Report, 26, 1-16.

Dafflon, B. and W. Barrash, 2012, Three-dimensional stochastic estimation of porosity distribution: Benefits of using ground-penetrating radar velocity tomograms in simulated-annealing-based or Bayesian sequential simulation approaches: Water Resources Research, 48(5), 1-11, doi: 10.1029/2011WR010916.

Dafflon, B., J. Irving, and K. Holliger, 2009, Simulated-annealing-based conditional simulation for the local-scale characterization of heterogeneous aquifers: Journal of Applied Geophysics, 68(1), 60-70, doi: 10.1016/j.jappgeo.2008.09.010.

Dafflon, B., J. Irving, and W. Barrash, 2011, Inversion of multiple intersecting high-resolution crosshole GPR profiles for hydrological characterization at the Boise Hydrogeophysical Research Site: Journal of Applied Geophysics, 73(4), 305-314, doi: 10.1016/j.jappgeo.2011.02.001.

Deparis, J., and S. Garambois, 2009, On the use of dispersive APVO GPR curves for thin-bed properties estimation: Theory and application to fracture characterization: Geophysics, 74(1), J1-J12, doi: 10.1190/1.3008545.

Dolan, S., and C. J. Bean, 1997, Some remarks on the estimation of fractal scaling parameters from borehole wire-line logs: Geophysical Research Letters, 24(10), 1271-1274, doi: 10.1029/97GL00987.

de Figueiredo L. P., D. Grana, F. L. Bordignon, M. Santos, M. Roisenberg, and B. B. Rodrigues, 2018, Joint Bayesian inversion based on rock-physics prior modeling for the estimation of spatially correlated reservoir properties: Geophysics, 83(5), M49-M61, doi: 10.1190/geo2017-0463.1.

Forte, E. and Pipan, M., 2017, Review of multi-offset GPR applications: Data acquisition, processing and analysis: Signal Processing, 132, 210-220, doi: 10.1016/j.sigpro.2016.04.011.

Frankel, A., and R. W. Clayton, 1986, Finite difference simulations of seismic scattering: Implications for the propagation of short-period seismic waves in the crust and models of crustal heterogeneity: Journal of Geophysical Research, 91(B6), 6465-6489, doi: 10.1029/JB091iB06p06465.

Giannopoulos, A., 2005, Modelling ground penetrating radar by gprMax: Construction and Building Materials, 19(10), 755-762, doi: 10.1016/j.conbuildmat.2005.06.007.

Gibson, B.S. and Levander, A.R., 1990, Apparent layering in common-midpoint stacked images of two-dimensionally heterogeneous targets: Geophysics, 55(11), 1466-1477, doi: 10.1190/1.1442794.

Goff, J.A., and T.H. Jordan, 1988, Stochastic modeling of seafloor morphology: Inversion of sea beam data for second-order statistics: Journal of Geophysical Research: Solid Earth, 93(B11), 13589-13608, doi: 10.1029/JB093iB11p13589.

Greaves, R. J., D.P. Lesmes, J.M. Lee, and M. N. Toksöz, 1996, Velocity variations and water content estimated from multi-offset, ground-penetrating radar: Geophysics, 61(3), 683-695, doi: 10.1190/1.1443996.

Gueting, N., A. Klotzsche, J. van der Kruk, J. Vanderborght, H. Vereecken, and A. Englert, 2015, Imaging and characterization of facies heterogeneity in an alluvial aquifer using GPR full-waveform inversion and cone penetration tests: Journal of Hydrology, 524, 680-695, doi: 10.1016/j.jhydrol.2015.03.030.

Hartzell, S., S. Harmsen, and A. Frankel, 2010, Effects of 3D random correlated velocity perturbations on predicted ground motions: Bulletin of the Seismological Society of America, 100(4), 1415-1426, doi: 10.1785/0120090060.

Hochstetler, D. L., W. Barrash, C. Leven, M. Cardiff, F. Chidichimo, and P. K. Kitanidis, 2016, Hydraulic tomography: continuity and discontinuity of high-K and low-K zones: Groundwater, 54(2), 171-185, doi: 10.1111/gwat.12344.

Holliger, K., Levander, A., Carbonell, R. and Hobbs, R., 1994, Some attributes of wavefields scattered from Ivrea-type lower crust: Tectonophysics, 232(1-4), 267-279, doi: 10.1016/0040-1951(94)90089-2.

Hubbard, S., and N. Linde, 2010, Hydrogeophysics, in P. A. Wilderer, ed., Treatise on Water Science: Elsevier, 401-434.

Hu, B. X., M. M. Meerschaert, W. Barrash, D. W. Hyndman, C. He, X. Li, and L. Guo, 2009, Examining the influence of heterogeneous porosity fields on conservative solute transport: Journal of Contaminant Hydrology, 108(3-4), 77-88, doi: 10.1016/j.jconhyd.2009.06.001.

Ikelle, L. T., S.K. Yung, and F. Daube, 1993, 2-D random media with ellipsoidal autocorrelation functions: Geophysics, 58(9), 1359-1372, doi: 10.1190/1.1443518.

Irving, J., R. Knight, and K. Holliger, 2009, Estimation of the lateral correlation structure of subsurface water content from surface-based ground-penetrating radar reflection images: Water Resources Research, 45(12), 1-14, doi: 10.1029/2008WR007471.

Irving, J., and K. Holliger, 2010, Geostatistical inversion of seismic and ground-penetrating radar reflection images: What can we actually resolve?: Geophysical Research Letters, 37(21), 1-5, doi: 10.1029/2010GL044852.

Johnson, D. S., C. R. Aragon, L. A. McGeoch, and C. Schevon, 1991, Optimization by simulated annealing: An experimental evaluation; part II, graph coloring and number partitioning: Operations Research, 39(3), 378-406, doi: 10.1287/opre.39.3.378.

Jones, A. G., and K. Holliger, 1997, Spectral analyses of the KTB sonic and density logs using robust nonparametric methods: Journal of Geophysical Research: Solid Earth, 102(B8), 18391-18403, doi: 10.1029/96JB03668.

Kelkar, M., Perez, G. and Chopra, A., 2002, Applied Geostatistics for Reservoir Characterization: Society of Petroleum Engineers.

Knight, R., 2001, Ground penetrating radar for environmental applications: Annual Review of Earth and Planetary Sciences, 29(1), 229-255, doi: 10.1146/annurev.earth.29.1.229.

Kobr, M., S. Mareš, and F. Paillet, 2005, Geophysical well logging in hydrogeophysics, in Y. Rubin and S. Hubbard, eds., Hydrogeophysics: Springer, 291-331, doi: 10.1007/1-4020-3102-5_10.

Lauzon, D., and D. Marcotte, 2019, Calibration of random fields by FFTMA-SA: Computers & Geosciences, 127, 99-110, doi: 10.1016/j.cageo.2019.03.003.

Lavoué, F., Brossier, R., Métivier, L., Garambois, S. and Virieux, J., 2014, Two-dimensional permittivity and conductivity imaging by full waveform inversion of multioffset GPR data: A frequency-domain quasi-Newton approach: Geophysical Journal International, 197(1), 248-268, doi: 10.1093/gji/ggt528.

Leven, C., and P. Dietrich, 2006, What information can we get from pumping tests? Comparing pumping test configurations using sensitivity coefficients: Journal of Hydrology, 319, 199-215, doi: 10.1016/j.jhydrol.2005.06.030.

Le Ravalec-Dupin, M., L.Y. Hu, and F. Roggero, 2008. Reconstruction of existing reservoir model for its calibration to dynamic data: Earth Science Frontiers, 15(1), 176-186, doi: 10.1016/S1872-5791(08)60020-2.

Le Ravalec, M., B. Noetinger, and L. Hu, 2000, The FFT moving average generator: An efficient numerical method for generating and conditioning Gaussian simulations: Mathematical Geology, 32(6), 701-722, doi: 10.1023/A:1007542406333.

Le Ravalec-Dupin, M., B. Coureaud, L. Nicolas, and F. Roggero, 2004, Conditioning an underground gas storage site to well pressures: Oil & Gas Science and Technology, 59(6), 611-624, doi: 10.2516/ogst:2004044.

Le Ravalec, M., and E. Mouche, 2012, Calibrating transmissivities from piezometric heads with the gradual deformation method: an application to the Culebra Dolomite Unit at the Waste Isolation Pilot Plant (WIPP), New Mexico, USA: Journal of Hydrology, 472, 1-13, doi: 10.1016/j.jhydrol.2012.08.053.

Liang, M., D. Marcotte, and P. Shamsipour, 2016, Simulation of nonlinear coregionalization models by FFTMA: Computers & Geosciences, 89, 220-231, doi: 10.1016/j.cageo.2016.01.005.

Liu, Y., Z. Shi, B. Wang, and T. Yu, 2018, GPR impedance inversion for imaging and characterization of buried archaeological remains: A case study at Mudu city cite in Suzhou, China: Journal of Applied Geophysics, 148, 226-233, doi: 10.1016/j.jappgeo.2017.12.002.

Maliva, R.G., 2016, Aquifer Characterization Techniques: Springer.

Mangel, A.R., Moysey, S.M. and Bradford, J., 2020, Reflection tomography of time-lapse GPR data for studying dynamic unsaturated flow phenomena: Hydrology and Earth System Sciences, 24(1), 159–167, doi: 10.5194/hess-24-159-2020.

Mount, G.J., Comas, X. and Cunningham, K.J., 2014, Characterization of the porosity distribution in the upper part of the karst Biscayne aquifer using common offset ground penetrating radar, Everglades National Park, Florida: Journal of Hydrology, 515, 223-236, doi: 10.1016/j.jhydrol.2014.04.048.

Nichols, J., D. Mikesell, and K. Van Wijk, 2010, Application of the virtual refraction to near-surface characterization at the Boise Hydrogeophysical Research Site: Geophysical Prospecting, 58(6), 1011-1021, doi: 10.1111/j.1365-2478.2010.00881.x.

Nussbaumer, R., N. Linde, G. Mariethoz, and K. Holliger, 2019, Simulation of fine-scale electrical conductivity fields using resolution-limited tomograms and area-to-point kriging: Geophysical Journal International, 218(2), 1322-1335, doi: 10.1093/gji/ggz185.

Oliver, D. S., 1995, Moving averages for Gaussian simulation in two and three dimensions: Mathematical Geology, 27(8), 939-960, doi: 10.1007/BF02091660.

Romero-Ruiz, A., N. Linde, T. Keller, and D. Or, 2018, A review of geophysical methods for soil structure characterization: Reviews of Geophysics, 56(4), 672-697, doi: 10.1029/2018RG000611.

Rubin, Y., and S. Hubbard, 2006, Hydrogeophysics: Springer.

Salamon, P., D. Fernàndez-Garcia, and J. J. Gómez-Hernández, 2007, Modeling tracer transport at the MADE site: the importance of heterogeneity: Water Resources Research, 43(8), 1-15, doi: 10.1029/2006WR005522.

Schmelzbach, C., J. Tronicke, and Dietrich, P., 2012, High-resolution water content estimation from surface-based ground-penetrating radar reflection data by impedance inversion: Water Resources Research, 48(8), 1-16, doi: 10.1029/2012WR011955.

Schön, J. H., 1998, Physical Properties of Rocks: Fundamentals and Principles of Petrophysics: Pergamon Press.

Stolt, R. H., 1978, Migration by Fourier transform, Geophysics: 43(1), 23-48, doi: 10.1190/1.1440826.

Tronicke, J., K. Holliger, W. Barrash, and M. D. Knoll, 2004, Multivariate analysis of crosshole georadar velocity and attenuation tomograms for aquifer zonation: Water Resources Research, 40(1), 1-14, doi: 10.1029/2003WR002031.

Tronicke, J., and K. Holliger, 2005, Quantitative integration of hydrogeophysical data: Conditional geostatistical simulation for characterizing heterogeneous alluvial aquifers: Geophysics, 70(3), H1-H10, doi: 10.1190/1.1925744.

Xu, Z., J. Irving, K. Lindsay, J. H. Bradford, P. Zhu, and K. Holliger, 2020a, Estimation of the 3D correlation structure of an alluvial aquifer from surface-based multi-frequency ground-penetrating radar reflection data: Geophysical Prospecting, 68(2), 678-689, doi: 10.1111/1365-2478.12857.

Xu, Z., J. Irving, Y. Liu, P. Zhu, and K. Holliger, 2020b, Conditional stochastic inversion of common-offset GPR reflection data: SEG Technical Program Expanded Abstracts, 3567-3671, doi: 10.1190/segam2020-3427578.1.

Yang, X., and P. Zhu, 2017, Stochastic seismic inversion based on an improved local gradual deformation method: Computers & Geosciences, 109, 75-86, doi: 10.1016/j.cageo.2017.08.010.

Yilmaz, Ö., 2001, Seismic Data Analysis: Processing, Inversion, and Interpretation of Seismic Data: SEG.

Yuan, H., Montazeri, M., Looms, M.C. and Nielsen, L., 2019, Diffraction imaging of ground-penetrating radar data: Geophysics, 84(3), H1-H12, doi: 10.1190/geo2018-0269.1.

Zeng, Z., X. Chen, J. Li, L. Chen, Q. Lu, and F. Liu, 2015, Recursive impedance inversion of ground-penetrating radar data in stochastic media: Applied Geophysics, 12(4), 615-625, doi: 10.1007/s11770-015-0514-0.

FIGURE CAPTIONS

Figure 1: Workflow summarizing the proposed conditional stochastic inversion procedure for generating a single output realization.

Figure 2: Synthetic porosity model with dashed vertical lines denoting the prescribed borehole locations.

Figure 3: (a) Processed synthetic GPR section corresponding to the porosity model from Figure 2 and (b) the estimated and true source wavelets in blue and red, respectively. The dashed vertical red lines in (a) show the considered borehole locations.

Figure 4: Generation of a single conditional stochastic porosity realization for our synthetic example using the method summarized in equation 3. Shown are (a) $Z^*$, the ordinary-kriging-based estimate of porosity based on the porosity log values along boreholes BH-1 and BH-3; (b) $Z_u$, an unconditional stochastic porosity realization generated using the FFT-MA method; (c) $Z_u^*$, the ordinary-kriging-based estimate of porosity based on the unconditional porosity values from (b) at the borehole locations; and (d) $Z_u$, the final conditional realization.

Figure 5: Comparison of (a) the true porosity model from Figure 2 with (b), (c), and (d) three stochastic realizations obtained using our inversion methodology. Also shown are (e) the mean and (f) the standard deviation obtained from 100 of such realizations.

Figure 6: Comparison of (a) porosity profiles at the central borehole location shown in Figure 2, and (b) corresponding GPR traces. The red lines show the observed data, whereas the gray and blue lines show the results for 100 inverted realizations and their mean, respectively. Also plotted in (c) are the "prior" porosity curves at the central borehole location corresponding to 100 conditional stochastic realizations that were not constrained to fit the GPR data (gray), along with their mean (blue) and the true porosity values (red).

Figure 7. Location of BHRS wellfield in relation to the Boise River. The dashed blue line joining wells C6, A1, and C3 corresponds to the considered surface-based GPR reflection survey.

Figure 8: (a) Processed GPR section from the BHRS and (b) the corresponding estimated source wavelet. The dashed vertical red lines in (a) show the borehole locations.

Figure 9: Porosity logs obtained along BHRS boreholes (a) C6, (b) A1, and (c) C3. The upper and lower dashed red lines indicate the depth of the groundwater table and penetration limit of the GPR data, respectively.

Figure 10: (a) and (b) Two stochastic realizations of porosity along the BHRS profile obtained using our inversion methodology; (c) and (d) mean and standard deviation inferred from 100 of such stochastic realizations, respectively.

Figure 11: Comparison of (a) porosity profiles at the central borehole location shown in Figure 8, and (b) corresponding GPR traces. The red lines show the observed data, whereas the gray and blue lines show the results for 100 inverted realizations and their mean, respectively. Also plotted in (c) are the "prior" porosity curves at the central borehole location corresponding to 100 conditional stochastic realizations that were not constrained to fit the GPR data (gray), along with their mean (blue) and the measured porosity log data (red).

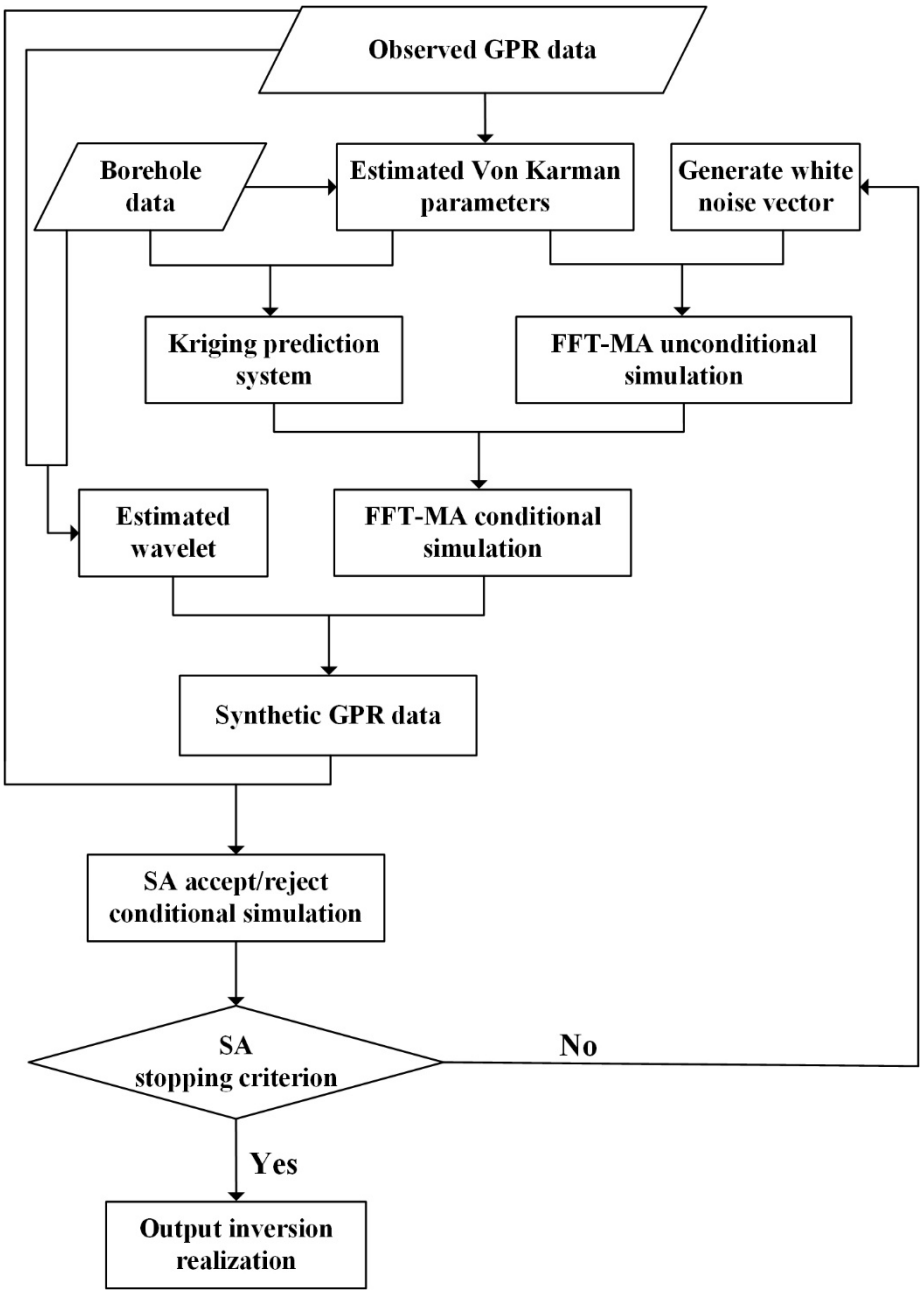


Figure 1: Workflow summarizing the proposed conditional stochastic inversion procedure for generating a single output realization.

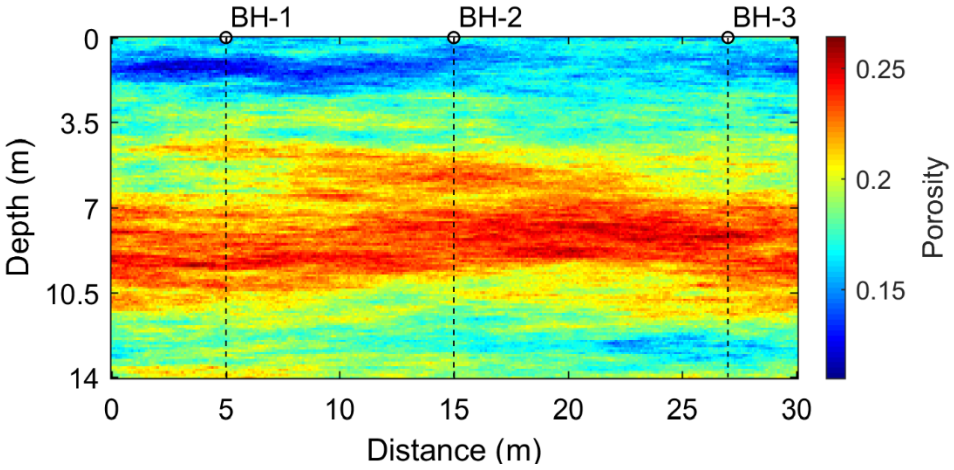


b

Figure 2: Synthetic porosity model with dashed vertical lines denoting the prescribed borehole locations.

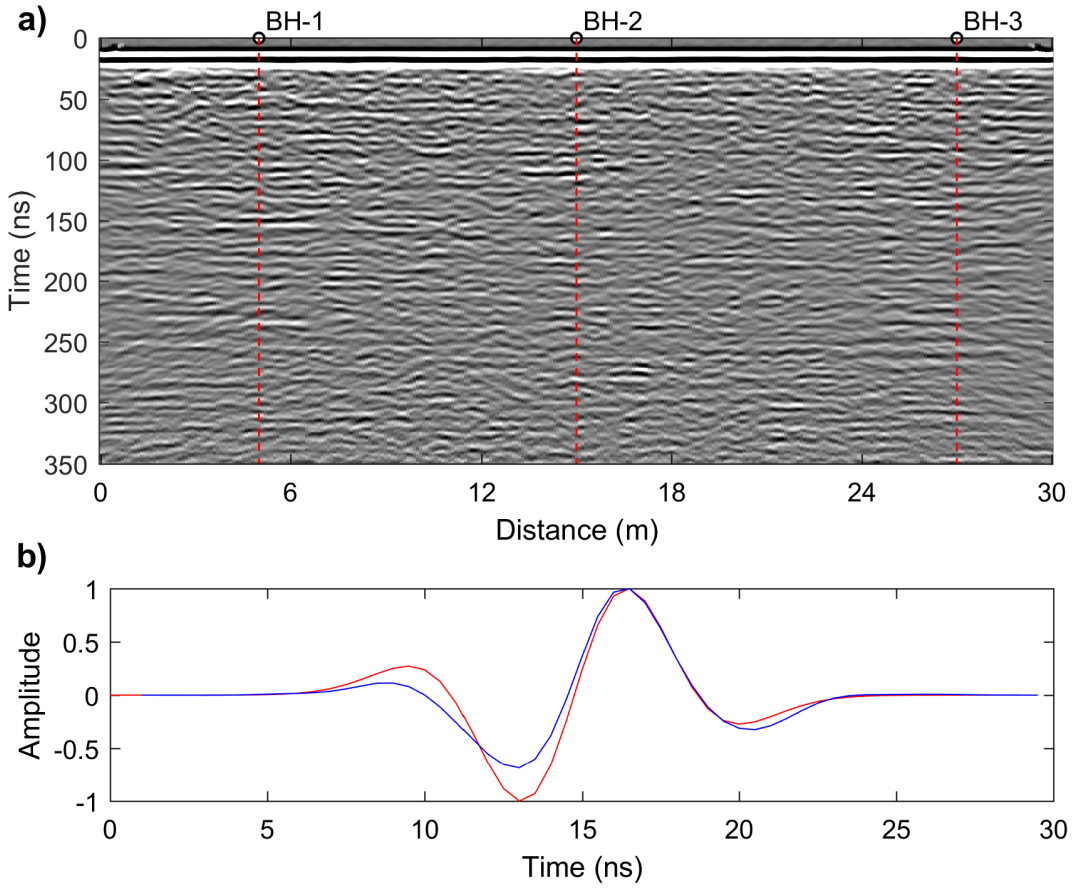


Figure 3: (a) Processed synthetic GPR section corresponding to the porosity model from Figure 2 and (b) the estimated and true source wavelets in blue and red, respectively. The dashed vertical red lines in (a) show the considered borehole locations.

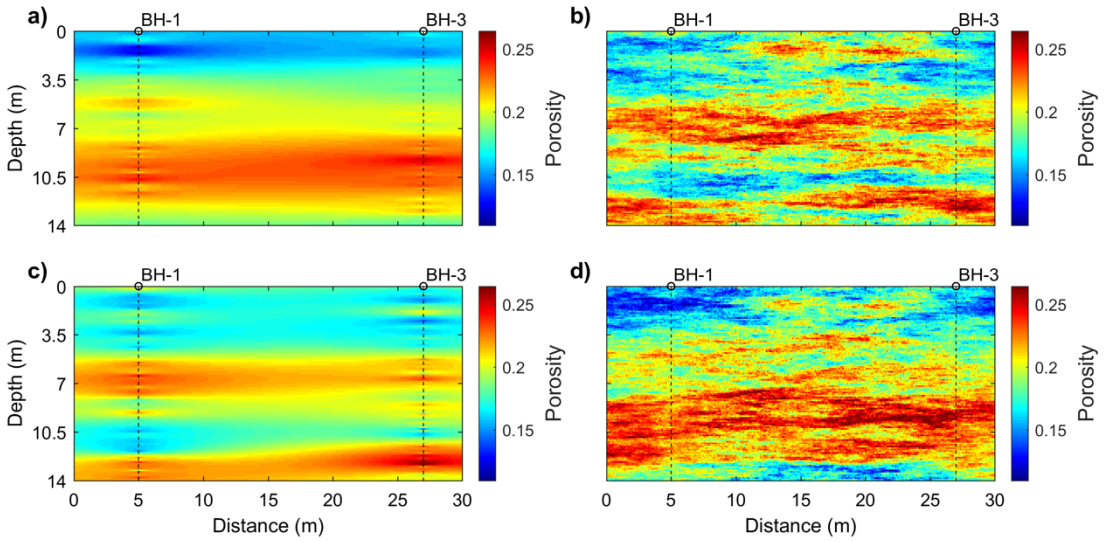


Figure 4: Generation of a single conditional stochastic porosity realization for our synthetic example using the method summarized in equation 3. Shown are (a) $Z^*$, the ordinary-kriging-based estimate of porosity based on the porosity-log values along boreholes BH-1 and BH-3; (b) $Z_u$, an unconditional stochastic porosity realization generated using the FFT-MA method; (c) $Z_u^*$, the ordinary-kriging-based estimate of porosity based on the unconditional porosity values from (b) at the borehole locations; and (d) $Z_u$, the final conditional realization.

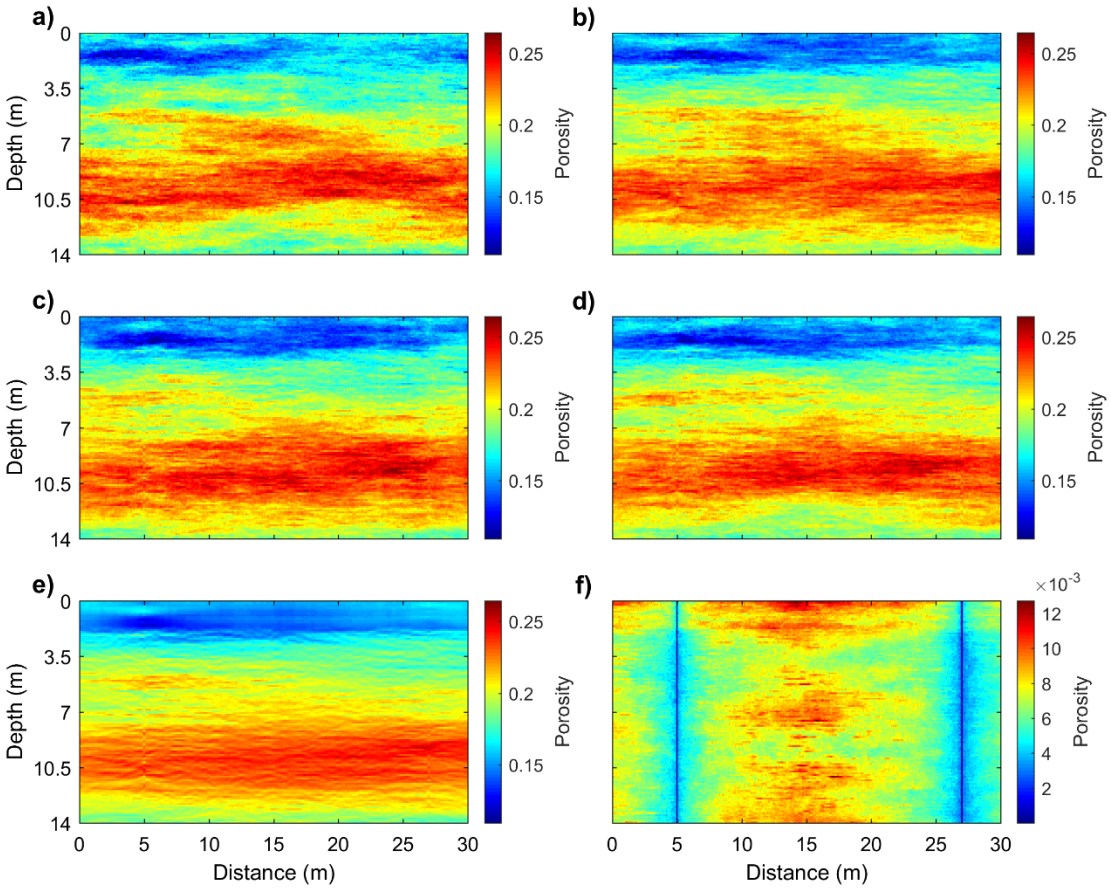


Figure 5: Comparison of (a) the true porosity model from Figure 2 with (b), (c), and (d) three stochastic realizations obtained using our inversion methodology. Also shown are (e) the mean and (f) the standard deviation obtained from 100 of such realizations.

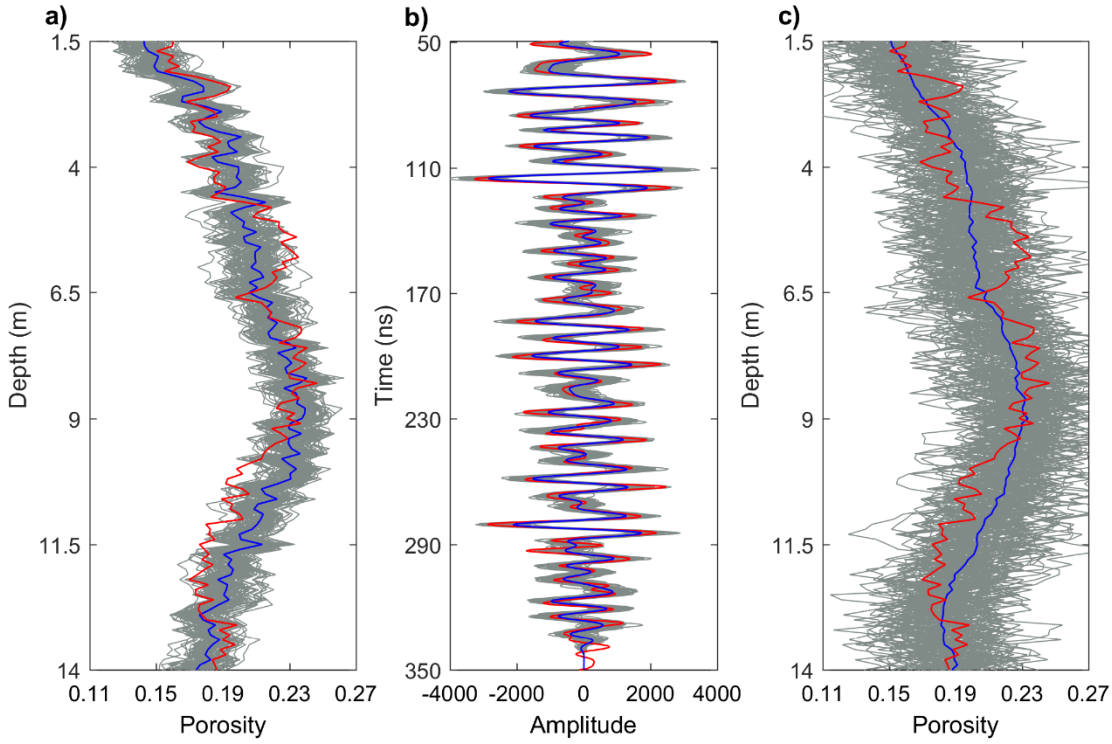


Figure 6: Comparison of (a) porosity profiles at the central borehole location shown in Figure 2, and (b) corresponding GPR traces. The red lines show the observed data, whereas the gray and blue lines show the results for 100 inverted realizations and their mean, respectively. Also plotted in (c) are the "prior" porosity curves at the central borehole location corresponding to 100 conditional stochastic realizations that were not constrained to fit the GPR data (gray), along with their mean (blue) and the true porosity values (red).

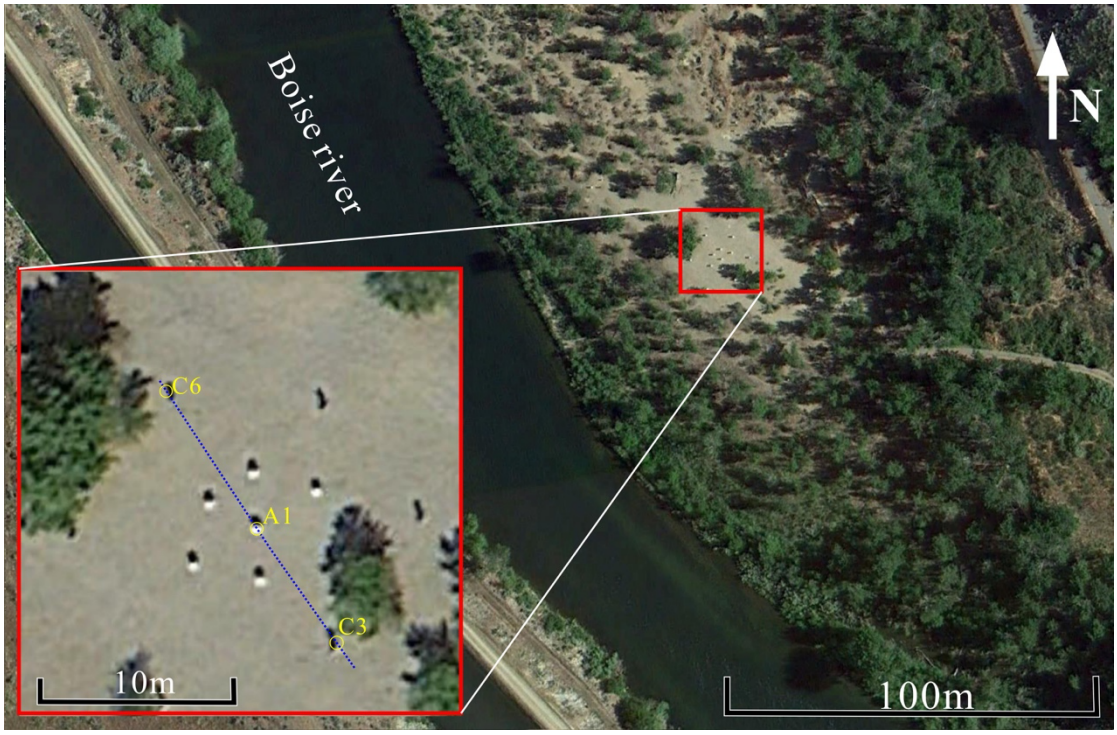


Figure 7. Location of BHRS wellfield in relation to the Boise River. The dashed blue line joining wells C6, A1, and C3 corresponds to the considered surface-based GPR reflection survey.

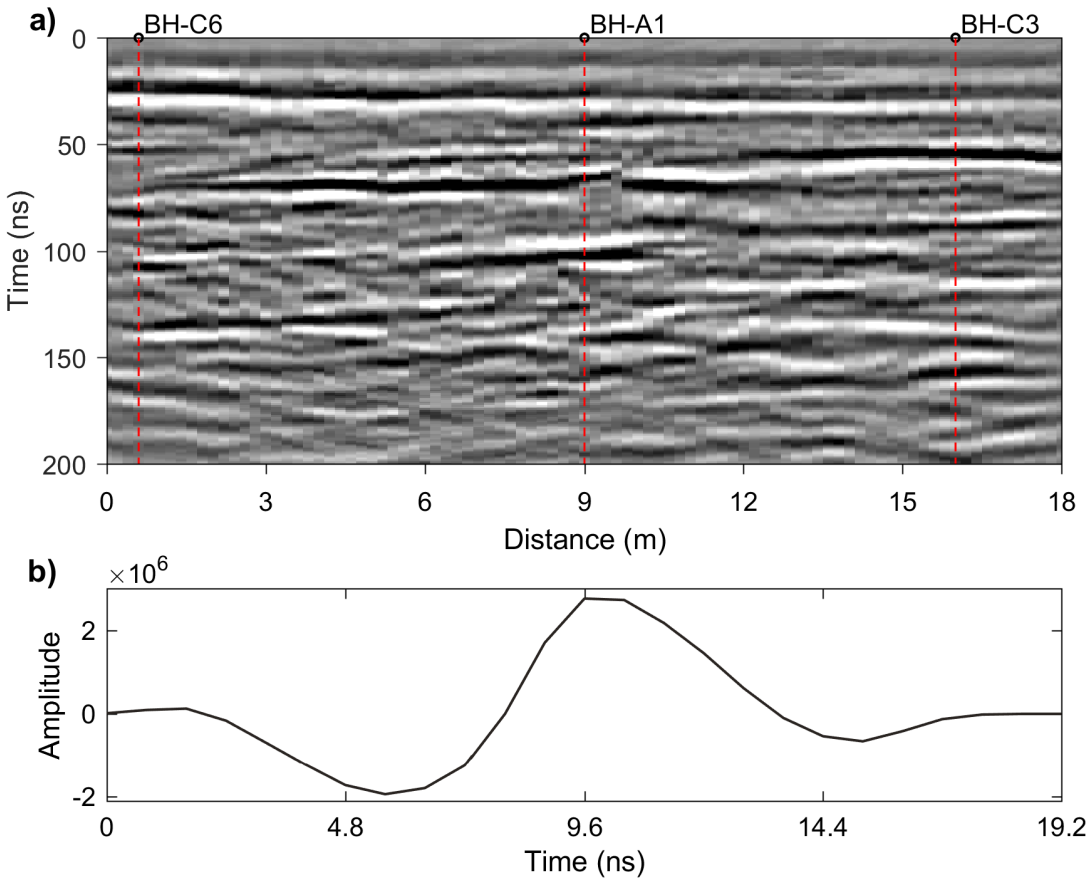


Figure 8: (a) Processed GPR section from the BHRS and (b) the corresponding estimated source wavelet. The dashed vertical red lines in (a) show the borehole locations.

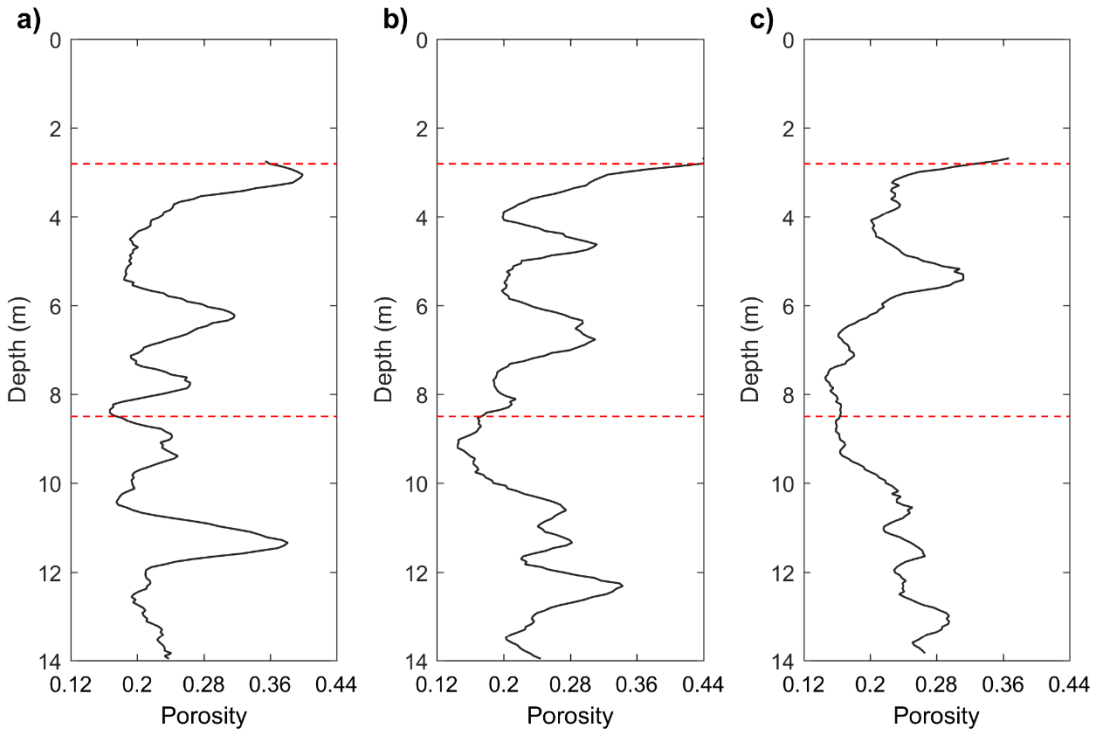


Figure 9: Porosity logs obtained along BHRS boreholes (a) C6, (b) A1, and (c) C3. The upper and lower dashed red lines indicate the depth of the groundwater table and penetration limit of the GPR data, respectively.

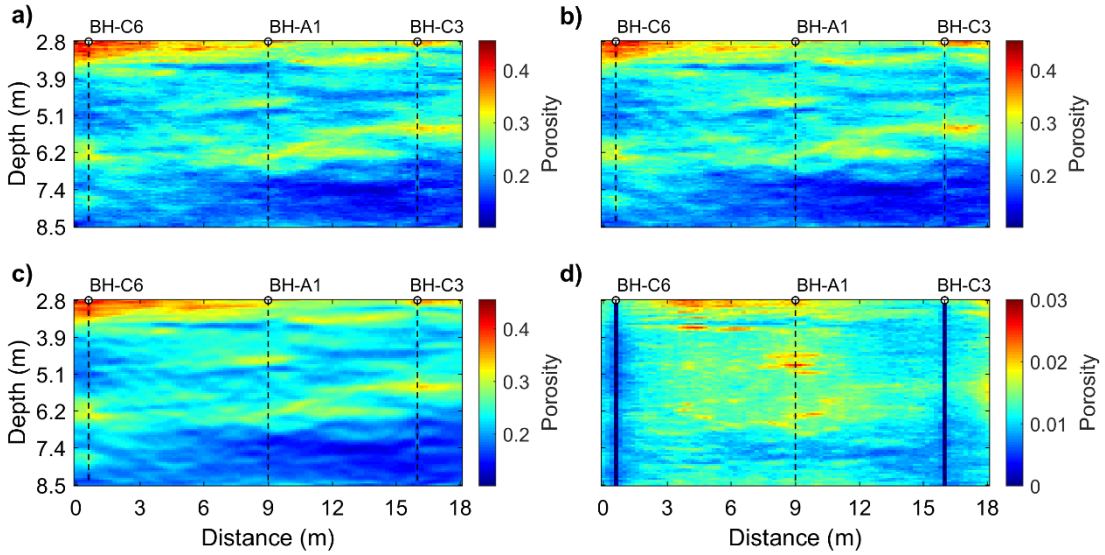


Figure 10: (a) and (b) Two stochastic realizations of porosity along the BHRS profile obtained using our inversion methodology; (c) and (d) mean and standard deviation inferred from 100 of such stochastic realizations, respectively.

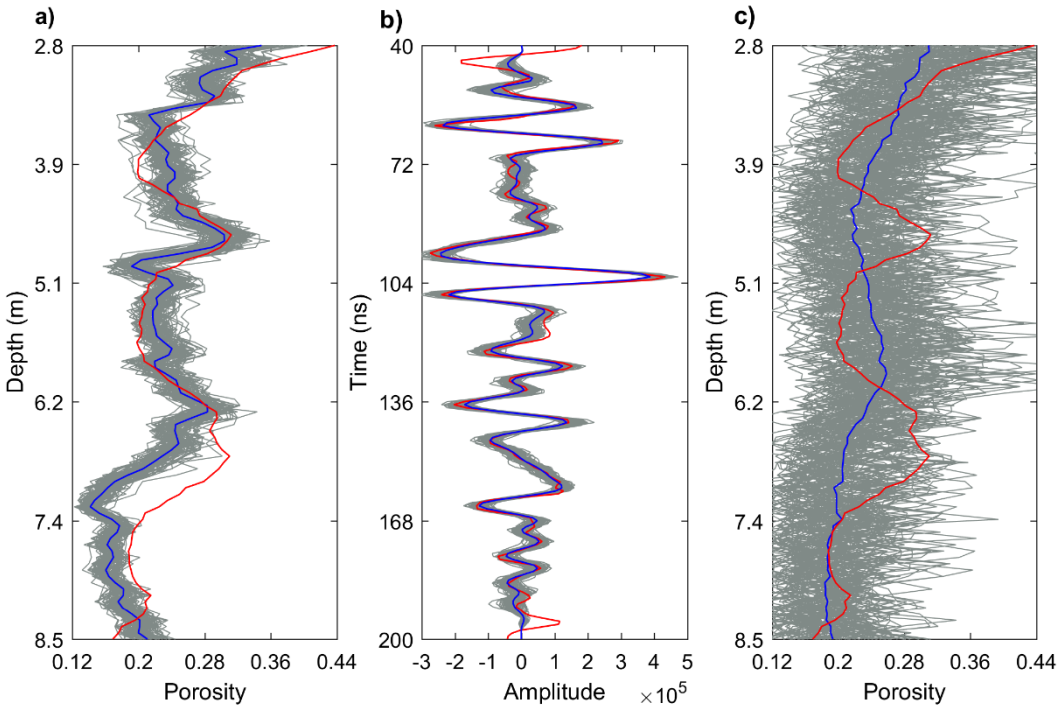


Figure 11: Comparison of (a) porosity profiles at the central borehole location shown in Figure 8, and (b) corresponding GPR traces. The red lines show the observed data, whereas the gray and blue lines show the results for 100 inverted realizations and their mean, respectively. Also plotted in (c) are the "prior" porosity curves at the central borehole location corresponding to 100 conditional stochastic realizations that were not constrained to fit the GPR data (gray), along with their mean (blue) and the measured porosity-log data (red).